

Self-Assembled Plasmonic Coaxial Nanocavities for High-Definition Broad-Angle Coloring in Reflection and Transmission

Haibin Ni,* Alexey V. Krasavin, Lu Zhang, An Ping, Chao Pan, Jianxin Cheng, Ming Wang, Jianhua Chang,* and Anatoly V. Zayats*

Resonant spectral scattering from metallic nanostructures is an attractive alternative approach to produce colors instead of using chemical pigments. Here, a technological platform based on self-assembled arrays of coaxial plasmonic resonators is developed for generating a bright color gamut over the entire visible spectral range in both reflection and transmission, offering the potential for ultrahigh definition coloring over large areas. Unlike the approaches using the nanostructure periodicity to define colors, the developed method employs color engineering based on the localized plasmon resonances in nanocavities, therefore, providing a broad angular response and viewing angles of up to 40°. With the nanoscale dimensions of color pixels and an increased viewing angle range, the proposed approach allows achieving large-area color patterns with local coloring controlled by post-processing, important for display technology, anticounterfeiting and artistic applications.

1. Introduction

Color definition employing resonant spectral properties of metallic nanostructures related to the excitation of surface plasmons have shown a strong potential for the realization of high-density environmental-friendly displays with

long lifetimes.^[1] Outperforming the traditional approaches based on pigments with ink-spot sizes of around $\approx 20 \mu\text{m}$ and a print resolution of around 1000 dots per inch (DPI) and extending already impressive capabilities of all-dielectric approaches,^[2] plasmonic nanostructures can confine visible light to subwavelength dimensions, and hence offer an opportunity to dramatically decrease the pixel size and achieve higher DPI, as well as tunable colors.^[3] Approaches for plasmonic color formation can be divided into two families: one relying on a periodicity of nanostructures and another employing resonances of individual nanostructures.^[3c] The former includes wavelength-selective transmission through nanohole or nanoslit arrays, and resonant interaction

of light with arrays of coupled nanoparticles or metal-insulator-metal (MIM) nanostructures.^[4] In this case, the obtained coloring is angle-dependent and a certain number of periods is needed to achieve the effect, therefore, requiring pixel sizes of a few micrometers, despite the arrays are made of subwavelength elements.^[3a,c,4c,5] The latter approach is usually realized employing small isolated metallic nanoparticles with plasmonic resonances and, therefore, the spectral response and the produced colors dependent on the size, shape, and material composition.^[3b,c,6] In this case, the pixels can be ultimately small being defined by the size of the nanoparticle and seen as a diffraction limited spot, but the intensity of light scattered by individual nanostructures is usually not strong enough to be clearly seen in the bright-field, especially when they are deposited directly on a transparent substrate.^[3b,7] The introduction of a back-reflector below the nanoparticles helps to increase the scattering efficiency in reflection sacrificing coloring in the transmitted light. In this geometry, various nanocavity-based plasmonic antennas, such as nanodisks on a film,^[1a,3b] MIM nanocavities with varied insulator gaps,^[8] nanorod and nanotrench structures^[9] have been demonstrated with an ultimately small pixel size leading to image resolution more than 100 000 DPI, a broad and bright color gamut together with high tolerance to the viewing angle.^[10] Utilizing the combined action of specular and diffused reflections, the capabilities of nanostructured

Dr. H. Ni, L. Zhang, A. Ping, C. Pan, J. Cheng, Prof. J. Chang
Jiangsu Key Laboratory of Meteorological Observation and Information Processing
School of Electronic and Information Engineering
Nanjing University of Information Science & Technology
Nanjing 210044, P. R. China
E-mail: nihaibin@nuist.edu.cn; jianhuachang@nuist.edu.cn

Dr. A. V. Krasavin, Prof. A. V. Zayats
Department of Physics and London Centre for Nanotechnology
King's College London
Strand, London WC2R 2LS, UK
E-mail: a.zayats@kcl.ac.uk

Prof. M. Wang
Jiangsu Key Laboratory on Optoelectronic Technology
School of Physical Science and Technology
Nanjing Normal University
Nanjing 210023, P. R. China

 The ORCID identification number(s) for the author(s) of this article can be found under <https://doi.org/10.1002/adom.202001923>.

DOI: 10.1002/adom.202001923

plasmonic surfaces were further extended to introduce 3D effects.^[9a,11] Engineering the phase of the reflected or transmitted light opens up the possibilities for its spatial control and the realization of flat lenses, deflectors, or holograms.^[12]

Self-assembly methods have significant advantages over the low-throughput techniques based on electron beam lithography and allow fabrication of large areas of nanostructures at a low cost. In terms of color definition, the self-assembled nanostructures have so far either low resolution (being based on a periodicity or randomization)^[13] or offer a very limited color range.^[14]

In this work, we employ a self-assembly fabrication technique based on nanosphere lithography together with engineering of the multiple plasmonic resonances in metal coaxial nanocavities and nanoapertures to demonstrate color definition covering the entire visible spectrum in both reflection and transmission. The underlining mode engineering approach based on cylindrical surface plasmons in the coaxial nanostructures increases the absorption efficiency and ensures robust color definition over a broad angular spectrum of illumination and observation. The color of the resulting pixels can be controlled via local post-processing, while the nanoscale size of the underlying nanostructures offers the potential of achieving the ultimate image resolution, restricted only by the diffraction limit. The applications may range from high-definition displays and high-density data storage to anticounterfeiting and artistic designs.

2. Nanostructure Design and Principle of Operation

2.1. Coaxial Nanocavity Array

Schematic diagrams of arrays of coaxial nanostructures with tuned geometry and spectral response are shown in **Figure 1**. Coaxial nanocavity arrays were fabricated by nanosphere lithography (see the Experimental Section for the details). Polystyrene (PS) latex nanospheres were self-assembled in a highly ordered hexagonal array on a silica substrate, followed by their partial etching using reactive ion etching (RIE). An Ag film was then deposited on the top of the structure to produce an array of nanocavities (Figure 1c). The subwavelength size of the nanocavities (diameter in the range of 10–60 nm) ensures that the ultimate observed pixel size is only limited by the diffraction. Each nanocavity in the array is formed by a dielectric ring protruding into the metal film and acts as a resonator selecting the frequency of the coupled light. The resonant frequencies, defined by the geometrical parameters of the structure, determine the spectrum of the reflected light (transmission is negligible in this case). Particularly, the spectral response is defined by the excitation of cylindrical surface plasmon (CSP) resonances on both inner and outer walls of the cylindrical nanocavity.^[15] When the gap width W is decreased to tens of nanometers, as realized in the studied nanostructures, the CSP resonances become coupled to produce

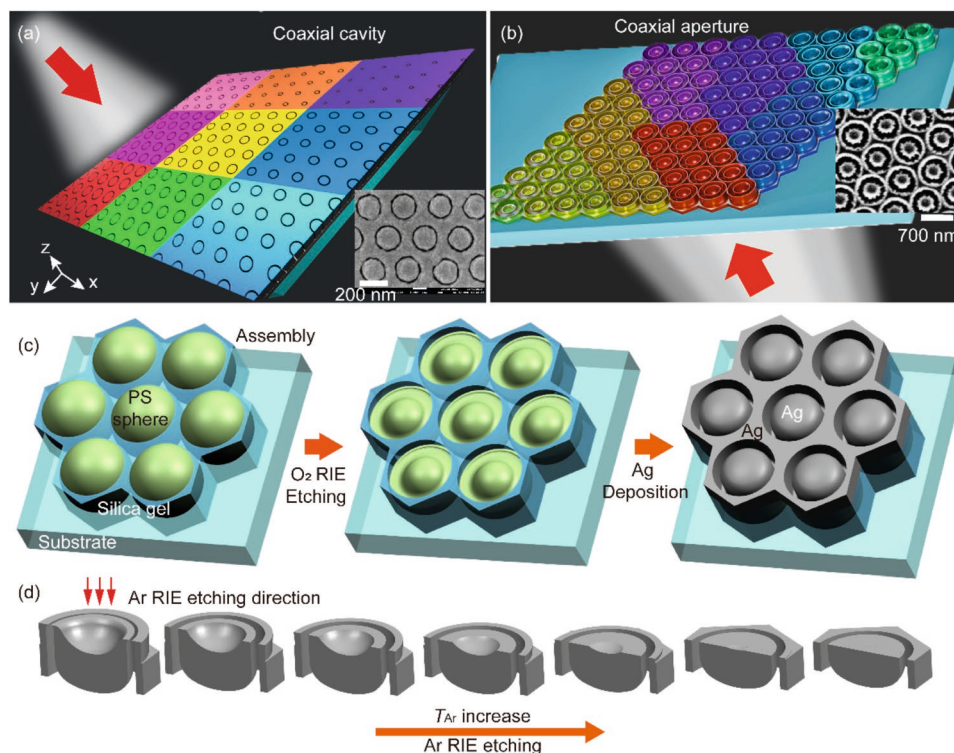


Figure 1. a) Schematic diagram of the coaxial nanocavity arrays with tuned parameters encoding colors. Inset: a scanning electron microscopy (SEM) image of a coaxial nanocavity array with $R = 100$ nm, $W = 10$ nm, $H = 100$ nm, $d = 70$ nm and $P = 250$ nm (compare with the final fabrication stage in (c)). b) Schematic diagram of the coaxial nanoaperture arrays. Inset: An SEM image of a nanoaperture array with $R = 280$ nm, $W = 100$ nm, $H = 150$ nm, $d = 100$ nm, and $P = 690$ nm (compare with unit cell images at short T_{Ar} times in (d)). c) Schematic of the fabrication process workflow for the coaxial cavity arrays. d) Morphology evolution of the coaxial nanoaperture under Ar milling with increasing time T_{Ar} . Red arrows indicate RIE milling direction. See the Experimental Section for details.

a gap MIM-type cylindrical mode (g-CSP).^[16] While the surface plasmon mode in each nanocavity can be treated as a localized mode, the structure can also support delocalized surface plasmon polaritons (SPPs), particularly the SPP Bloch modes (SPP-BW), when the arrays are highly ordered at long distances.

2.2. Coaxial Nanoaperture Array

Besides engineering colors in reflection, color management in a transmission mode is also widely used in displays, filters, and windows.^[17] To address these applications, coaxial nanoaperture arrays with high transmission can be produced from their coaxial nanocavity counterparts (see the Experimental Section for details), preserving the CSP-based optical properties and hence providing tunable colors in the transmission mode. To achieve this, the coaxial nanocavity arrays were coated with a layer of polyurethane (PU) polymer and peeled off from the substrate. Then, the PU film was turned upside down and glued to another glass slide. Finally, the sample was milled using RIE to form the coaxial nanoaperture array. Depending on the milling, which changes the height of the coaxial nanocavity, the resulting structure exhibits different colors, as illustrated in Figure 1b,d.

2.3. Principle of Color Definition

Geometrical parameters of the coaxial nanocavity R , W , and H (shown in Figure 2a), as well as composition materials determine the resonant frequencies of the supported g-CSP modes and therefore the color of light reflected from the nanocavity arrays or transmitted through the coaxial nanoaperture arrays.^[18] The excited g-CSP modes (Figure 2b) are characterized by highly

enhanced electric field in the coaxial gaps (Figure 2c–f). Upon illumination, the g-CSP modes that satisfy boundary conditions in the axial and azimuthal directions of the coaxial nanocavity are excited. Particularly, the g-CSP mode should fulfill a Fabry–Perot-type phase matching condition in the axial direction

$$\left| 2Hk_{g\text{-CSP}}(\omega) + \Delta\theta_1 + \Delta\theta_2 \right| = 2\pi m \quad (1)$$

where $\Delta\theta_1$ and $\Delta\theta_2$ are the phase changes upon the mode reflection at the top and bottom interfaces, respectively, $k_{g\text{-CSP}}(\omega)$ is the wave vector of the g-CSP mode and m is an integer describing the mode order in the vertical direction.^[5g,18] Beside this relation, the mode should also fulfill the azimuthal phase matching condition

$$2\pi Rk_{g\text{-CSP}}(\omega) = 2\pi n \quad (2)$$

where n is an integer, describing the corresponding mode order. By engineering the dispersion of the g-CSP modes via the variation of the nanocavity/nanoaperture geometrical parameters, reflection/transmission resonances at predesigned wavelengths can be achieved. Under the resonant conditions, the light at the prescribed wavelength is strongly absorbed due to the loss in the metal, resulting in the removal of these wavelengths from the nanostructure reflection/scattering spectrum, therefore providing the control of the color in both reflection and transmission over the whole visible range.

Delocalized SPP-BW modes may also be excited and supported by the entire array; their optical frequencies are additionally defined by the array periodicity.^[4a] Together, SPP-BW and g-CSP resonances determine the final observed colors. However, as will be seen below, for the designed parameters, the coloring is primarily defined by g-CSP modes ensuring angle independent performance and a diffraction-limited size of the observed color pixels.

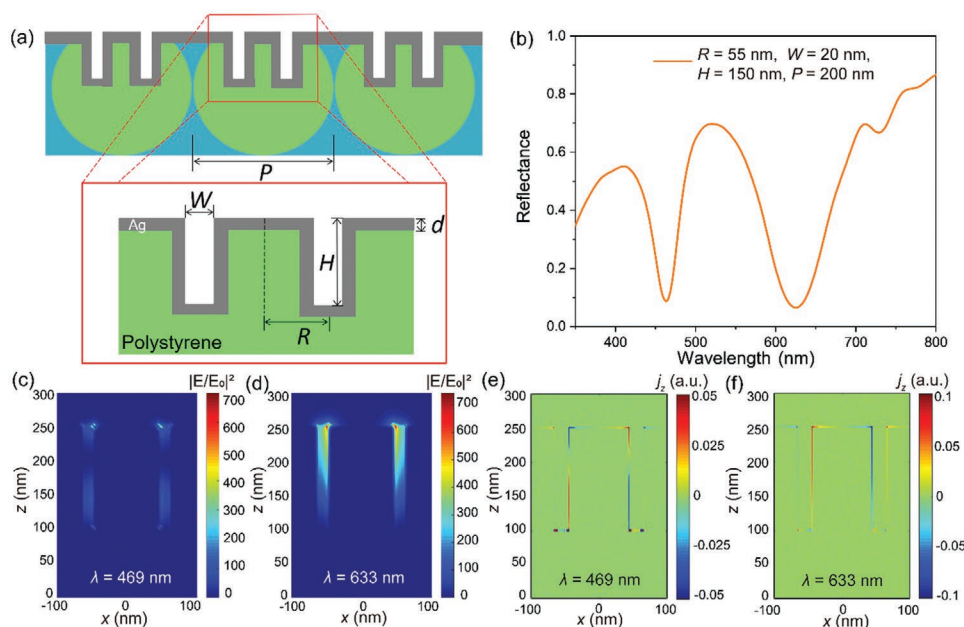


Figure 2. a) An idealized unit-cell cross-section of the coaxial nanocavities with indicated geometrical parameters. b) Typical simulated reflection spectrum of a coaxial nanocavity array with $R = 55$ nm, $W = 20$ nm, $H = 150$ nm and $P = 200$ nm. c,d) Electric field intensity and e,f) distributions of the z -component of the current density in the xz -plane at 469 and 633 nm wavelengths, corresponding to the reflection dips in (b).

3. Results and Discussion

3.1. Color Management with Coaxial Nanocavity Arrays in Reflection

Coaxial nanocavity arrays with varied geometry designed using the principles described above and produced by the nanosphere lithography over the large areas (at least $10 \times 10 \text{ mm}^2$) display colors which cover the whole visible range (Figure 3a–d).

Selective oxygen RIE etching with a time T_{O_2} defines at an initial fabrication stage R , W , and H parameters for different areas of the sample. Since the color is directly defined by geometry parameters of R , W , H , and P , we apply these four parameters to define the coaxial cavity design, while using the etching time T_{O_2} and metal film thickness d as the fabrication parameters. By choosing the thickness d of the deposited Ag film, H , R , and W can be continuously tuned, which results in the change in the reflected colors under the white light illumination (Figure 3b).

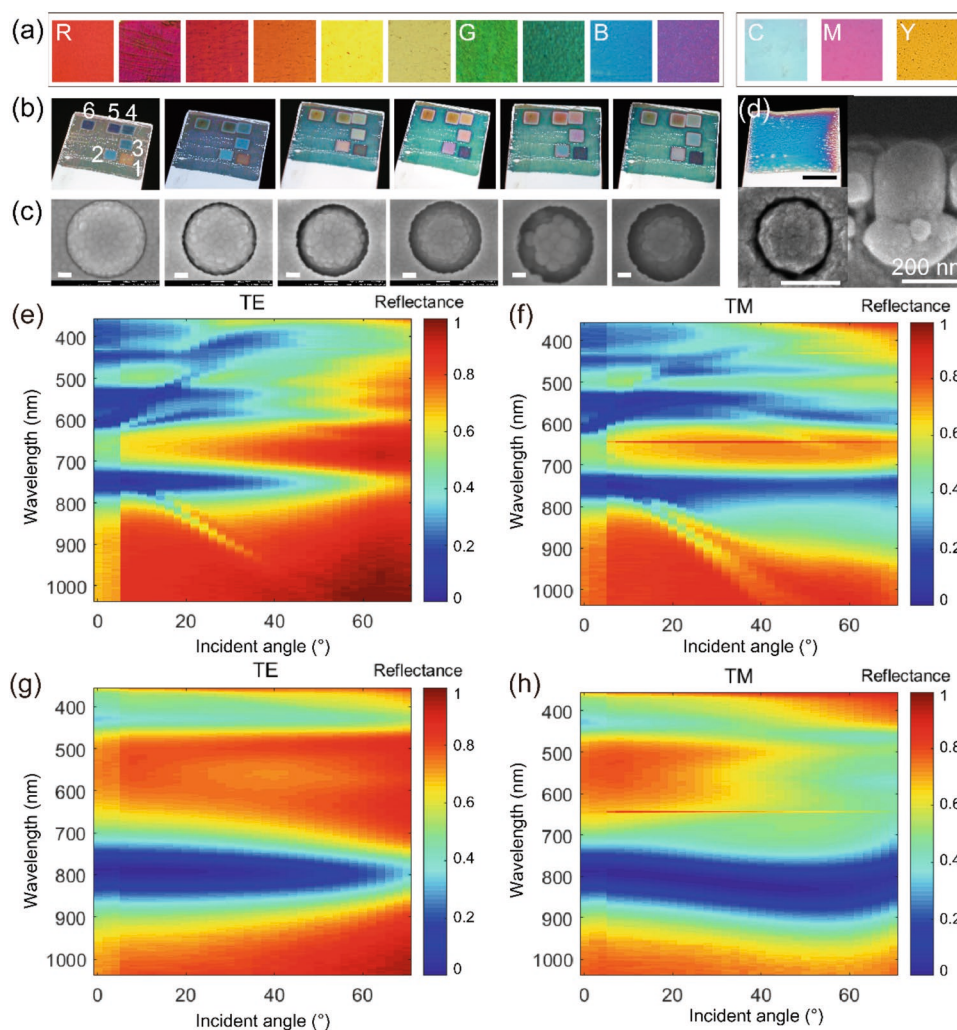


Figure 3. a) Reflection color photographs (each area $1 \times 1 \text{ mm}^2$) of the fabricated coaxial nanocavity arrays with $P = 690 \text{ nm}$ and W , H , and R simultaneously varied from 20 to 100 nm, from 100 to 400 nm and from 200 to 300 nm, respectively, during the fabrication process. b) Color photographs of six coaxial array areas with various initial states after RIE (marked with 1–6 on the left image) at subsequent stages of silver film deposition (images from left to right). The initial geometrical parameters for structures 1–6 in are: 1) $R = 325 \text{ nm}$, $W = 30 \text{ nm}$ and $H = 30 \text{ nm}$; 2) $R = 310 \text{ nm}$, $W = 60 \text{ nm}$ and $H = 58 \text{ nm}$; 3) $R = 295 \text{ nm}$, $W = 90 \text{ nm}$ and $H = 86 \text{ nm}$; 4) $R = 280 \text{ nm}$, $W = 120 \text{ nm}$ and $H = 114 \text{ nm}$; 5) $R = 265 \text{ nm}$, $W = 150 \text{ nm}$ and $H = 142 \text{ nm}$; 6) $R = 250 \text{ nm}$, $W = 180 \text{ nm}$ and $H = 170 \text{ nm}$; this corresponds to a simultaneous variation of the parameters from sample 1 to sample 6 with a step $\Delta R \approx -15 \text{ nm}$, $\Delta H \approx 28 \text{ nm}$ and $\Delta W \approx 30 \text{ nm}$; $P = 690 \text{ nm}$ is fixed for all six samples. Size of each square is $2 \text{ mm} \times 2 \text{ mm}$. Photographs from left to right demonstrate the changes of the coloring of the structures with a continuously increasing thickness of the sputtered Ag film d from 25 nm (first image on the left) to 150 nm (last image on the right) with a step of $\approx 25 \text{ nm}$, corresponding to simultaneous changes of $\Delta R \approx -6 \text{ nm}$, $\Delta W \approx -12 \text{ nm}$ and $\Delta H \approx 25 \text{ nm}$. c) SEM images of coaxial nanocavity arrays in areas 1–6 marked in (b) after sputtering a 150 nm thick Ag film. Scale bars are 100 nm in all the images. d) Optical and SEM images of the experimentally produced coaxial nanocavity arrays with $R = 105 \text{ nm}$, $W = 12 \text{ nm}$, $H = 100 \text{ nm}$ and $P = 250 \text{ nm}$. The scale bar is 5 mm in the CCD image and 200 nm in the SEM images. e–h) Experimentally measured angle-resolved reflection spectra of the coaxial nanocavity arrays for (e,g) TE- and (f,h) TM-polarized incident light for the samples with structural parameters: (e,f) $R = 250 \text{ nm}$, $W = 75 \text{ nm}$, $H = 375 \text{ nm}$, $P = 690 \text{ nm}$, $d = 225 \text{ nm}$ and (g,h) $R = 100 \text{ nm}$, $W = 15 \text{ nm}$, $H = 100 \text{ nm}$, $P = 250 \text{ nm}$, $d = 70 \text{ nm}$. The abrupt change at 5° is due to an unavoidable minor change of the light spot position at small angles.

Morphology evolution of the coaxial nanocavities with different initial geometric parameters but with the same metal film thickness ($d = 150$ nm Ag) clearly indicates the simultaneous tuning of R , W and H (Figure 3c) by the etching time T_{O_2} at the previous stage. As the etching time T_{O_2} increases, R decreases, while W and H increase. Furthermore, H is also partially determined by the thickness of the deposited film. The diameter of the spheres used in the fabrication determines the period of the array P (Figure 3d). One can see that with tuning the geometrical parameters of the nanocavity arrays during the fabrication process, both RGB and CMY color pallets can be realized.

The color of light reflected from the coaxial nanocavity arrays is produced by the subtraction of the resonant spectral bands from the white light illumination, therefore, it depends on both magnitudes and wavelength of the resonant reflection dips. This is controlled by the geometrical parameters and composition materials of the nanostructure. Before investigating the influence of the geometrical parameters on the reflected color, it is important to distinguish the role of g-CSP and SPP-BW modes. Reflecting the localized nature of the excited g-CSP modes, the broad and strong nondispersive resonances at 450, 560, and 750 nm in the angle-resolved reflection spectra (horizontal bands in Figure 3e,f) ensure that the produced color will not change with $\pm 40^\circ$ variation of the incident and observation angles. In addition to the g-CSP modes, much less pronounced dispersive SPP-BW modes, characterized by the narrow linewidths and shallow reflection dips (narrow inclined bands in Figure 3e,f), are also present in the reflection spectra, but they have an angular dependence defined by the SPP dispersion. At shorter wavelengths, there are noticeable anticrossing effects between the localized and propagating modes. At the same time, it is clear that the g-CSP modes dominate the coloring effects, while SPP-BW modes have a negligible effect on the color, which leads to the angle-independent performance.

Experimentally measured reflection maps show that the structures with shorter periods (Figure 3d) offer better color performance. The decrease of the periodicity to 250 nm can practically eliminate the effect from the SPP-BW modes in the visible by shifting the Bloch modes towards shorter wavelengths (Figure 3g,h). Additionally, the viewing angle range can be further increased to more than $\pm 60^\circ$. There is only one dominant reflection dip in the visible range for smaller coaxial nanocavities in such arrays, which makes it easy to tune the reflection color. Numerical simulation results further confirm such angle independent properties of the coaxial nanocavities (see Figure S1, Supporting Information). Due to the symmetry of the coaxial nanocavities, their spectral response is also independent on the in-plane angle (polarization) at normal incidence.

Engineering the spectral response through the geometrical parameters of the nanocavities and arranging them in a matrix of pixels one can produce an image or encode the information for the data storage. The defining role in the image resolution or the density of the stored data plays the pixel size, which crucially depends on a physical mechanism underlying the color formation. Since in the case of the nanocavities it is related to the excitation of localized g-CSP modes, supported by individual structures, each nanocavity works as a pixel. This leads to the possibility of the ultimately smallest pixel size

approaching the diffraction limit. With the fabrication technique demonstrated here employing 250 nm PS spheres, the resolution of the color display higher than 100 000 DPI can be achieved. The precision of the color definition depends on the ability of selective local modification of the related geometrical parameters. In the proposed approach, several mechanisms can be employed to achieve this: i) selective assembly of the PS spheres of different sizes, ii) locally selective RIE, or iii) selective plasmonic film deposition with controlled local thickness. Beyond self-assembly approaches, standard lithography methods or nanoimprint techniques can be used to define the cavities. Implementation of a multicolor pixel array via tuning the geometrical parameters of the nanocavities through selective etching (followed by the usual Ag film deposition) using a 30 μm Cu grid as a mask is demonstrated in Figure S2a in the Supporting Information. In addition, the ultimate resolution down to the size of a single nanostructure is presented in Figure S2b,c.

3.2. Numerical Optimization

Numerical simulations were used to further analyze the experimental findings and reveal the full potential of the proposed approach (see the Experimental Section for the details). Good agreement with the experimental results for $P = 250$ nm was obtained (Figure S3, Supporting Information), ensuring the feasibility of the geometry parametrization, and then a detailed study of the spectral response was performed. As it follows from the nature of the coaxial waveguide modes (Equations (1) and (2)), the resonant reflection dip continuously shifts to longer wavelength with the increase of R (Figure 4a) or H (Figure 4b) and the decrease of W (Figure 4c). Particularly for a period $P = 250$ nm, with the radius R increase from 15 to 65 nm, the reflection dip shifts in a very broad range from 380 to 650 nm, spanning the whole visible spectral range (Figure 4a). This gives the possibility to continuously vary the desired pixel color in the CMY gamut (Figure 4e). As was mentioned above, in practice the variation of the radius can be achieved by choosing the PS spheres of various diameters for the self-assembly and be further fine-tuned by the thickness of the deposited metal film. The same effect of scanning the reflection color can be achieved by varying the gap width W (Figure 4c), which can be controlled during the fabrication by choosing the etching time T_{O_2} or the thickness d of the metallic film. It is interesting to notice that the width of the reflection dip is relatively constant as R and H are varied (Figure 4a,b), while the dip broadens as W increases or P decreases (Figure 4c,d), most probably resulting from the fact that the resonances in the neighboring nanocavities become coupled with the decrease of the separation in the latter case and with the increase of out-of-nanocavity leakage in the former.

The evolution of the numerically simulated reflection spectra was transformed into colors according to the CIE 1931 xy color space chromaticity diagram (see the Experimental Section for the details). As the result, with the change of a single geometrical parameter R and the properly engineered design, the coaxial nanocavity arrays practically demonstrate tuning of the reflected color from yellow to magenta and then

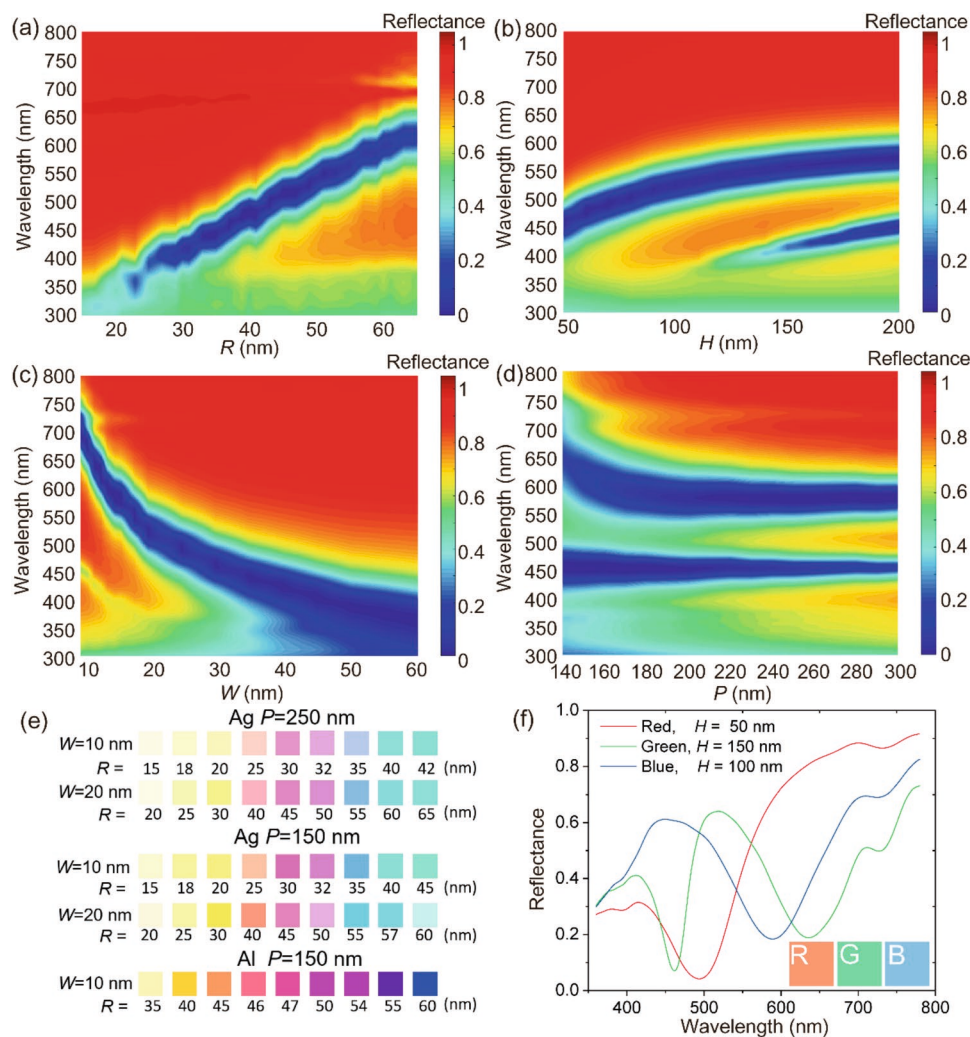


Figure 4. a–d) Numerically simulated reflection spectra for different (a) radii R , (b) heights H , (c) gap widths W , and (d) periodicities P for the coaxial nanocavity arrays in an Ag film. The fixed parameters (set of three in each case) in (a–d) are $R = 50$ nm, $W = 20$ nm, $H = 100$ nm, and $P = 250$ nm except for (d) where $H = 200$ nm. e) CMY color pallet produced by the color of coaxial nanocavity arrays with varied R , W and material composition, but with same $H = 100$ nm, obtained using numerical simulations (see the Experimental Section). f) RGB color pallet realized by varying the nanocavity height H with the corresponding reflection spectra $W = 20$ nm, $R = 51$ nm and $P = 150$ nm.

to cyan (Figure 4e). When W decreases from 20 to 10 nm, similar colors can be reproduced, again by only varying the radius R . This indicates that colors reflected from the coaxial nanocavities have high tolerance to the variation of the smallest nanostructure parameter (W) and, therefore, have broad allowances for the fabrication process. Periodicity P does not change the color dramatically when it changes from 250 to 150 nm. Even with a different plasmonic material (Al, which additionally is abundant and cheap), the coaxial nanocavity arrays still show a similar color evolution but with a minor difference attributed to the material properties as will be discussed below.

Due to the subtractive nature of the color formation, the CMY gamut is naturally and controllably reproduced by the nanocavity arrays through the excitation of individual absorptive plasmonic resonances. The RGB color gamut, on the other hand, is generally based on emissive colors. However, it is

possible to achieve a RGB-type pallet with absorptive plasmonic resonances or their collective action if they produce broad absorption bands. For example, in order to reproduce the red color in reflection, light in the entire visible spectral range should be absorbed except for the red wavelengths. In a similar manner, the blue color in reflection can be obtained. To realize the green color, two absorption resonances are needed in order to eliminate the visible light in the short- and long-wavelength spectral ranges with respect to the green one. Figure S4 in the Supporting Information shows the realization of the RGB pallet using a nanocavity array with $P = 200$ nm. A full scan of the spectral response in the R – H parameter space performed for a smaller period $P = 150$ nm shows that the RGB gamut can be reproduced with a change of a single parameter H at $R = 51$ nm and $W = 20$ nm (Figure 4f), which is experimentally feasible. This is achieved taking the advantage of a continuous shift of a broad plasmonic resonance through the entire visible

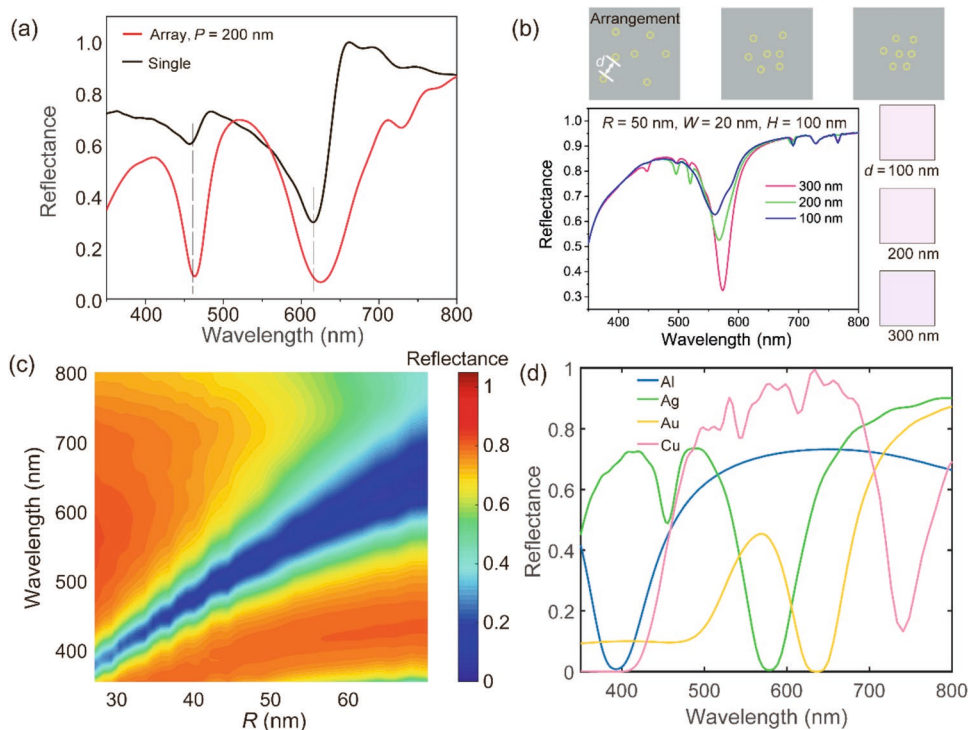


Figure 5. a) Comparison between the numerically simulated reflection spectra of a periodic coaxial nanocavity array ($R = 55$ nm, $W = 20$ nm, $H = 150$ nm, $P = 200$ nm) and a single coaxial nanocavity with the same parameters. b) Schematic diagram of coaxial nanocavities located at random positions with average distances about 300, 200, and 100 nm, together with the corresponding numerically simulated reflection spectra. On the basis of the simulated spectra, the colors presented to the right of the graph were obtained. c) Numerically simulated reflection spectra of the Al coaxial nanocavity arrays with $R = 28$ – 68 nm, $W = 8$ nm, $H = 100$ nm and $P = 250$ nm. d) Numerically simulated reflection spectra of the coaxial nanocavity arrays with the same $R = 35$ nm, $W = 10$ nm, $H = 100$ nm, $P = 150$ nm realized with various metallic materials.

spectrum, initially absorbing all the wavelengths except red, then except blue, and, finally, with the appearance of a higher-order plasmonic resonance in the short-wavelength range, additionally blocking blue again (Figures S4 and S5, Supporting Information). Overall, the experimentally measured (Figure 3) and numerically calculated (Figure 4; Figure S5a, Supporting Information) spectral dependences agree with each other and show that the efficiency of coupling of the incident light to plasmonic resonances can reach values higher than 90% (corresponding to less than 10% reflection), with a baseline reflection level of 70%.

Finally, the localized nature of the g-CSP modes was confirmed in the numerical investigation of the reflection spectrum as a function of the period. As illustrated in Figure 4d, the positions of both reflection dips do not shift with the variation of P from ≈ 180 to 300 nm, signifying the fact that the transmission spectrum and, therefore, the encoded color are efficiently defined by the properties of the individual nanocavities (the slight spectral shift of the long-wavelength resonance at smaller periods is most probably related to the onset of coupling of the neighboring modes). This is further confirmed by the simulation results for an isolated coaxial nanocavity. The reflection dips corresponding to the excitation of the localized g-CSP modes keep the same wavelength positions as in the case of the array, though experiencing a decrease in the magnitude (Figure 5a).

3.3. Random Nanocavities

As some coupling between the localized modes in the nanocavities was observed when they are closely packed in an ordered array, signified by the broadening of the dips in Figure 4c,d as well as the slight shift of one resonance in Figure 4d, more insight into this effect can be gained investigating the color generated by randomly located coaxial nanocavities. Simulated reflectance spectra of such structures with an average distance between the nanocavities around 300, 200, and 100 nm are presented in Figure 5b. For a fair comparison all nanostructures had seven nanocavities and the reflection in all three cases was normalized to the light power incident on a $1.5 \mu\text{m} \times 1.5 \mu\text{m}$ area. Similarly to the effect observed in the periodic arrays, when the distance between neighboring nanocavities becomes smaller than 200 nm, coupling between the nanocavities grows stronger, leading to slight broadening of the reflection dip with no change in the dip position; overall this produces only a minor change in the observed color (Figure 5b). On one hand, it further confirms the robust behavior of the localized g-CSP modes with respect to the change of the distances between the nanocavities and, on the other hand, demonstrates the stability of the developed approach for color encoding even with randomly distributed coaxial nanocavities and, therefore, tolerances in the fabrication process.

3.4. Material Dependence

Besides using silver as a plasmonic material, we further calculated the colors reflected from the same coaxial nanocavity arrays in an aluminum film (Figure 5c), as this material is abundant and the structures made from it are more stable.^[19] The aluminum arrays showed similar evolution in the CMY regime with the single reflection dip spanning through the entire visible spectral region upon the change of the nanocavity radius, which demonstrates the mass-production potential of the approach (Figure 4e). The linewidth of the resonant reflection dip is another important factor that affects the resulting color. The linewidth of a surface plasmon resonance, underlying it, is determined by both Ohmic and radiation losses, which can be described by the relation $1/\tau_{\text{tot}} = 1/\tau_{\text{ohmic}} + 1/\tau_{\text{rad}}$, where τ_{tot} , τ_{ohmic} , and τ_{rad} are the total decay time and the decay times corresponding to Ohmic and radiation losses, respectively. Thus, in addition to the shape and the geometrical parameters of the structure, τ_{ohmic} and τ_{rad} are additional parameters that can be tuned through the change of the plasmonic material, which affect both loss experienced by the mode and its radiation properties through the material optical constants.

Coaxial nanocavities made from other plasmonic materials were also numerically studied (Figure 5d). Diverse optical properties of these materials (both plasma frequencies and the presence/position of interband transitions) provide the opportunity to engineer the reflected colors using the material-related degree of freedom. For example, using aluminum-based arrays, it is possible to produce a deeper blue color due to a broad and steep reflection dip across a 500–720 nm range (Figure 4e).

3.5. Dependence of Reflected Colors on Fabrication Tolerances

It is inevitable that there will be discrepancies between the nominal design and the real fabricated samples in terms of a change of the nanostructure geometry present in all the nanostructures (characteristic to the fabrication method) and the variation of the geometry among individual structures, leading to a certain spread of geometrical parameters in the assembly. All of this can affect the optical performance of the array. Having in mind prospective fabrication of the samples by a nanoimprint method, the color tolerance of the coaxial nanocavity arrays was evaluated in terms of an unintended variation of the gap width, characteristic to this technique. Keeping the nominal radius R and bottom width W constant, the gap width was symmetrically increased towards the top with a decrease of an internal radius r , varied from 45 nm, corresponding to the nominal structure with vertical walls, to 35 nm. In such noncylindrical nanocavities, both resonances in the reflection spectrum (designed to produce a green color) experience a shift of around 50 nm (Figure 6). Although there is a noticeable color evolution, it can be accounted for by changing the nominal geometrical parameters to adjust for the particular characteristics of the implemented nanoimprint process.

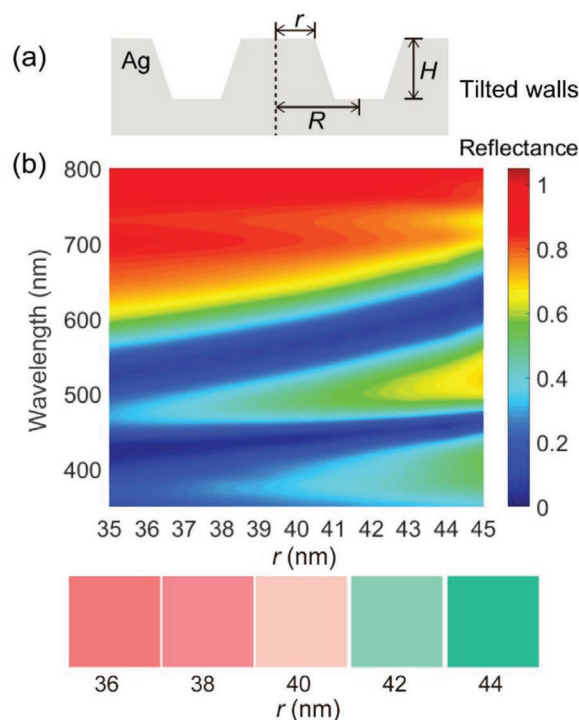


Figure 6. a) Schematic cross section of a coaxial nanocavity with tilted side walls. b) Spectral reflection as a function of the inner radius of the coaxial nanocavity r (indicated in (a)), varied from 45 nm (vertical walls) to 35 nm (tilted walls) with $R = 55$ nm, $W = 20$ nm, $H = 150$ nm, and $P = 200$ nm, together with the corresponding reflection colors.

3.6. Color Engineering for Transmitted Light

When the coaxial nanocavities are redeposited upside-down on another substrate and ion-etched from the backside to produce nanoapertures (see the Experimental Section for the details), the arrays can also be used to display colors in a transmission mode. SEM images of the fabricated coaxial nanoaperture arrays are presented in Figure 7a. The transmitted colors can be defined in the same way through engineering of the plasmonic modal profile of the nanostructure via variation of the nanostructure geometrical parameters, the origin of the plasmonic resonances determining the modal profile remains essentially unchanged. Particularly, the nanoaperture size (depth of the cavity) D was tuned by controlling the milling time T_{Ar} (Figure 1d). As the etching process continues, the slit width W increases and the sample shows a change of color in the transmission mode (Figure 7a–c, f–k). The color variation in transmission is complemented by the corresponding variation in reflection (Figure 7d). The experimentally measured and numerically simulated (Figure 7e) colors in transmission agree quite well. At the same time, the colors in reflection agree at smaller RIE times (12 min) and larger RIE times (30 min experimental color agrees with 33 min simulated color), but disagree in the middle RIE time range (12–18 min). The reason for this is that in numerical simulations it is very difficult to exactly implement the complex evolution of the nanostructure geometry during the RIE etching, including the geometry of the nanoaperture shallow inner cavity.

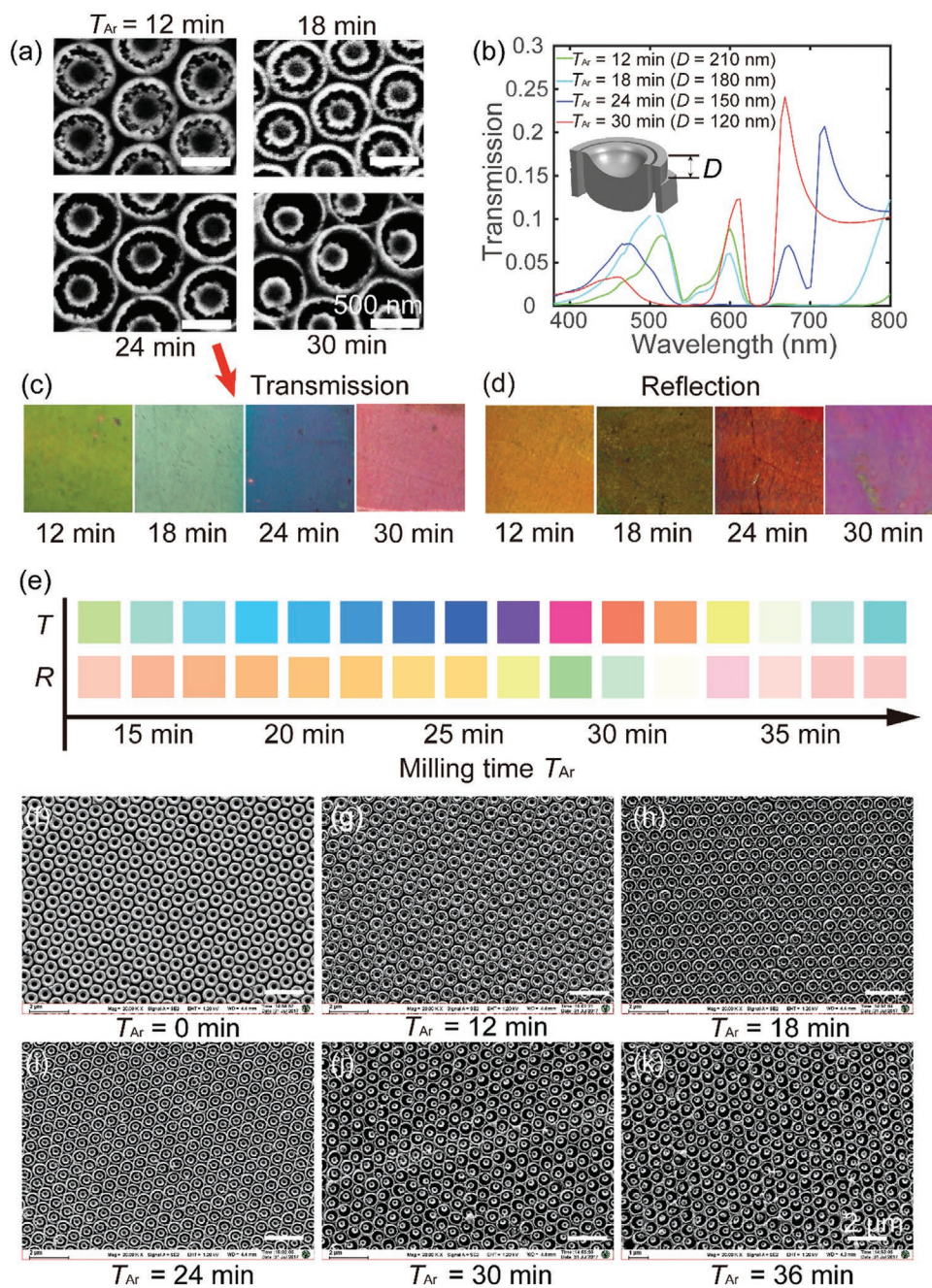


Figure 7. a) SEM images of the coaxial nanoaperture arrays with an increasing gap width. Scale bar is 500 nm in all images. b) Simulated transmission spectra of the coaxial nanoaperture arrays ($R = 210$ nm, $W = 160$ nm, $D = 270$ nm, $P = 690$ nm) corresponding to various milling times (leading to the decrease of D), calculated for etching speed of ≈ 5 nm min^{-1} . The inset shows the geometry of the cross section of the coaxial nanoaperture. c) Transmission and d) reflection images of the experimentally measured coaxial nanoaperture arrays for milling times (left-to-right) 12, 18, 24, and 30 min. The size of the squares is 2×2 mm 2 . e) Colors of the coaxial nanoaperture arrays in transmission and reflection obtained from the numerical simulations. f–k) SEM images showing the evolution of the nanostructure array during the milling process: (f) an initial backside surface morphology of the coaxial nanocavity array peeled off from the glass substrate; the surface morphology after (g) $T_{Ar} = 12$, (h) 18, (i) 24, (j) 30 and (k) 36 min of the reactive ion etching. The scale bar is 2 μm .

4. Conclusion

Bright coloring spanning through the entire visible spectral region both in reflection and transmission was achieved by engineering the plasmonic modes of the self-assembled arrays of coaxial nanocavities and nanoapertures. Colors can be

controlled through the straightforward variation of the geometrical parameters of the nanostructures at the fabrication stage or postprocessing. The color encoding based on localized plasmonic modes in individual nanostructures offers the prospect to realize pixels of ultimately small sizes approaching the diffraction limit, potentially providing an ultrahigh pixel density

and a display resolution of up to 100 000 DPI. Due to this mechanism, the color response of the designed nanostructures remains the same with the variation of the illumination and observation directions up to at least 40°, ensuring large viewing angles. The definition of CMY and RGB color pallets as well as many intermediate colors has been demonstrated. The implemented fabrication method allows high quality and large area manufacturing at a low cost. Overall, the proposed approach can be applied to realize high contrast, high resolution color displays,^[20] high density information storage,^[21] colorimetric sensors,^[22] and image encryption,^[23] as well as engineering of reflection, absorption or transmission spectra important for spectral filtering and selective excitation of hot-electrons.^[24]

5. Experimental Section

Fabrication of Coaxial Nanocavity Arrays: Monodisperse colloidal particles (polystyrene latex, nominal diameter $d = 250$ or 690 nm, polydispersity <10% from Bangs Laboratories Incorporated, used as received) were suspended uniformly in a water solution. Standard glass slides were cleaned with a 3:7 volume ratio solution of $H_2O_2:H_2SO_4$ for 1 h at 90 °C, which was followed by rinsing with DI water and drying with N_2 gas. The slides were treated with an oxygen plasma (Harrick Plasma Cleaner, PDC-002) under mild conditions for 10 min before use. 6 mL of DI water were added to the 20 μ L PS microsphere suspension with spheres of a 690 nm diameter and 20 μ L of a hydrolyzed tetraethylorthosilicate (TEOS) solution (98%, Sigma Aldrich). The resulting solution was sonicated for 5 min at room temperature to form the suspension for the assembly. The TEOS solution consisted of a 1:1:1.5 weight ratio of TEOS (98% Aldrich), 0.1 HCl, and ethanol (99.9%) and was stirred at room temperature for 1 h prior to use.^[25] A cleaned glass slide was partly vertically immersed into the mixed suspension and fixed. Then, the suspension was placed in an oven for evaporation at a temperature of $45 \text{ }^\circ\text{C} \pm 1 \text{ }^\circ\text{C}$. After the liquid components of the suspension were evaporated, a monolayer of ordered sphere arrays infiltrated with a silica gel was formed on the slide. For PS spheres of a 250 nm diameter, the concentrations of the spheres and TEOS solution, as well as the evaporation temperature need to be slightly adjusted to form high quality monolayer sphere arrays.

The substrates with the ordered sphere arrays infiltrated with the silica gel were treated with RIE with O_2 to achieve selective etching of the PS spheres. An Ag film (0.025 Torr, Ar, 2.5 sccm) was deposited on the sample at a rate of $\approx 0.4 \text{ nm s}^{-1}$ by magnetron sputtering (Jiashuo Vacuum Technology), the film thickness was monitored by a quartz oscillator. A 300 μ m thick Al_2O_3 slide (with a 2 mm \times 2 mm square opening aperture) was used as an RIE etching mask for selective etching of the monolayer of the ordered sphere array. The process gradually etches the nanospheres producing the nanocavity structures, the etching time can be varied to achieve the nanocavities with the desired geometrical parameters (Figure 1b). Morphology of the fabricated samples was characterized by scanning electron microscopy (JSM 7610F, JEOL). A thin layer of Pt was sputtered onto the samples to increase the conductivity of the sample surface when SEM characterization was performed (but not present during optical characterization).

Fabrication of Coaxial Nanoaperture Arrays: Initial coaxial nanocavity arrays were made by the method described in the previous section using 15 min O_2 etching and a 150 nm Ag film. Then, a 1 mm thick layer of NOA61 was coated on the top of the array and fully cured by UV light for 2 min. After this, the cured NOA61 film containing the Ag coaxial nanocavity arrays was peeled off from the substrate. RIE milling was used for etching the back side of the coaxial nanocavities to form coaxial nanoapertures. The etching parameters were: Ar, 20 sccm, pressure reactor 10 Pa, and 60 W RF power. The etching times were 12, 18, 24, 30, and 36 min, respectively, in order to control geometrical parameters. A 30 μ m Cu mesh with grid size of 120 μ m was used as RIE etching mask for selectively etching the sample to produce areas of different colors.

Spectral Characterization: Reflection spectra of the coaxial nanocavity arrays from 360 to 800 nm were measured by an optical spectrum analyzer (OSA, Ocean optics, USB 2000, 360–1100 nm) equipped with a 200 μ m core diameter reflection probe (Ocean Optics). A white light source (Yokogawa AQ4305, 50W) was coupled to six fibers in the reflection probe and was normally projected onto the surface of the coaxial nanocavity arrays; the reflected light was collected by another fiber in the bunch and sent to the OSA for detection. The measurements of angle resolved spectra were performed using an R1 device (Fuxiang Optics).

Simulation: Reflection and transmission spectra, electric field, and charge density distributions were simulated using a finite-difference time-domain method (Lumerical). Periodic boundary conditions were applied in the lateral directions, while in the direction perpendicular to the array perfectly matched layers (PMLs) were used. For the situations of a single nanostructure, PMLs were applied in all directions. A mesh size in all simulations was set to be 2 nm.

Color Transformation: The 1931 CIE standard color space was used to represent the simulated spectra as the produced colors. From the spectral power distribution I of the reflection spectra, XYZ values of the CIE can be determined using the formulas

$$X = \int_0^\infty I(\delta) \bar{x}(\delta) d\delta \quad (3)$$

$$Y = \int_0^\infty I(\delta) \bar{y}(\delta) d\delta \quad (4)$$

$$Z = \int_0^\infty I(\delta) \bar{z}(\delta) d\delta \quad (5)$$

In the XYZ parameter set of the CIE color space, Y indicates the brightness, and X and Z define the color itself. A CIE xy chromaticity graph is used to represent the obtained color map, where the coordinates x and y are calculated as

$$x = \frac{X}{X+Y+Z} \quad (6)$$

$$y = \frac{Y}{X+Y+Z} \quad (7)$$

Supporting Information

Supporting Information is available from the Wiley Online Library or from the author.

Acknowledgements

H.N. would like to thank National Natural Science Foundation of China (Grants 61605082 and 61875089), the Natural Science Foundation of Jiangsu Province (BK20160969, BE2016756), and the Priority Academic Program Development of Jiangsu Higher Education Institutions (PAPD). China Postdoctoral Science Foundation Funded Project (2017M611654). A.V.Z. and A.V.K. acknowledge the support from EPSRC UK (EP/M013812/1) and ERC iCOMM project (789340).

Conflict of Interest

The authors declare no conflict of interest.

Data Availability Statement

The data that support the findings of this study are available from the corresponding author upon reasonable request.

Keywords

angle-independent colors, coaxial nanocavities, high-definition colors, localized surface plasmons, nanoapertures

Received: November 7, 2020

Revised: February 15, 2021

Published online: March 18, 2021

- [1] a) A. S. Roberts, A. Pors, O. Albrektsen, S. I. Bozhevolnyi, *Nano Lett.* **2014**, *14*, 783; b) C. U. Hail, G. Schnoering, M. Damak, D. Poulidakos, H. Eghlidi, *ACS Nano* **2020**, *14*, 1783; c) Y. Bao, Y. Yu, H. Xu, C. Guo, J. Li, S. Sun, Z.-K. Zhou, C.-W. Qiu, X.-H. Wang, *Light Sci. Appl.* **2019**, *8*, 95.
- [2] W. Yang, S. Xiao, Q. Song, Y. Liu, Y. Wu, S. Wang, J. Yu, J. Han, D. P. Tsai, *Nat. Commun.* **2020**, *11*, 1864.
- [3] a) A. M. Shaltout, J. Kim, A. Boltasseva, V. M. Shalaev, A. V. Kildishev, *Nat. Commun.* **2018**, *9*, 2673; b) K. Kumar, H. Duan, R. S. Hegde, S. C. Koh, J. N. Wei, J. K. Yang, *Nat. Nanotechnol.* **2012**, *7*, 557; c) T. Chen, B. M. Reinhard, *Adv. Mater.* **2016**, *28*, 3522; d) N. J. Greybush, K. Charipar, J. A. Geldmeier, S. J. Bauman, P. Johns, J. Naciri, N. Charipar, K. Park, R. A. Vaia, J. Fontana, *ACS Nano* **2019**, *13*, 3875; e) X. Cui, X. Zhu, L. Shao, J. Wang, A. Kristensen, *Adv. Opt. Mater.* **2020**, *8*, 1901605; f) J. Zhao, M. Qiu, X. Yu, X. Yang, W. Jin, D. Lei, Y. Yu, *Adv. Opt. Mater.* **2019**, *7*, 1900646; g) S. Wu, Y. Ye, H. Duan, Y. Gu, L. Chen, *Adv. Opt. Mater.* **2019**, *7*, 1801302; h) J. S. Lee, J. Y. Park, Y. H. Kim, S. Jeon, O. Ouellette, E. H. Sargent, D. H. Kim, J. K. Hyun, *Nat. Commun.* **2019**, *10*, 4782; i) Y. J. Kim, Y. J. Yoo, G. J. Lee, D. E. Yoo, D. W. Lee, V. Siva, H. Song, I. S. Kang, Y. M. Song, *ACS Appl. Mater. Interfaces* **2019**, *11*, 11849.
- [4] a) L. Salomon, F. Grillot, A. V. Zayats, F. de Fornel, *Phys. Rev. Lett.* **2001**, *86*, 1110; b) S. Sun, Z. Zhou, C. Zhang, Y. Gao, Z. Duan, S. Xiao, Q. Song, *ACS Nano* **2017**, *11*, 4445; c) H. Wang, X. Wang, C. Yan, H. Zhao, J. Zhang, C. Santschi, O. J. F. Martin, *ACS Nano* **2017**, *11*, 4419; d) Y. Kim, K. Jung, J. Cho, J. K. Hyun, *ACS Nano* **2019**, *13*, 10717.
- [5] a) A. P. Ravishankar, M. A. van Tilburg, F. Vennberg, D. Visser, S. Anand, *Nanophotonics* **2019**, *8*, 1771; b) B. Yang, W. Liu, Z. Li, H. Cheng, S. Chen, J. Tian, *Adv. Opt. Mater.* **2018**, *6*, 1701009; c) S. Sun, W. Yang, C. Zhang, J. Jing, Y. Gao, X. Yu, Q. Song, S. Xiao, *ACS Nano* **2018**, *12*, 2151; d) X. Duan, N. Liu, *ACS Nano* **2018**, *12*, 8817; e) M. L. Tseng, J. Yang, M. Semmlinger, C. Zhang, P. Nordlander, N. J. Halas, *Nano Lett.* **2017**, *17*, 6034; f) V. Flauraud, M. Reyes, R. Paniagua-Domínguez, A. I. Kuznetsov, J. Brugger, *ACS Photonics* **2017**, *4*, 1913; g) Z. Dong, J. Ho, Y. F. Yu, Y. H. Fu, R. Paniagua-Domínguez, S. Wang, A. I. Kuznetsov, J. K. W. Yang, *Nano Lett.* **2017**, *17*, 7620; h) G. Wang, X. Chen, S. Liu, C. Wong, S. Chu, *ACS Nano* **2016**, *10*, 1788.
- [6] a) J. M. Guay, A. Cala Lesina, G. Cote, M. Charron, D. Poitras, L. Ramunno, P. Berini, A. Weck, *Nat. Commun.* **2017**, *8*, 16095; b) M. Ye, L. Sun, X. Hu, B. Shi, B. Zeng, L. Wang, J. Zhao, S. Yang, R. Tai, H. J. Fecht, J. Z. Jiang, D. X. Zhang, *Opt. Lett.* **2015**, *40*, 4979.
- [7] a) S. Y. Lee, C. Forestiere, A. J. Pasquale, J. Trevino, G. Walsh, P. Galli, M. Romagnoli, L. Dal Negro, *Opt. Express* **2011**, *19*, 23818; b) J. Olson, A. Manjavacas, L. Liu, W. S. Chang, B. Foerster, N. S. King, M. W. Knight, P. Nordlander, N. J. Halas, S. Link, *Proc. Natl. Acad. Sci. USA* **2014**, *111*, 14348.
- [8] C. Ji, S. Acharya, K. Yamada, S. Maldonado, L. J. Guo, *ACS Appl. Mater. Interfaces* **2019**, *11*, 29065.
- [9] a) D. J. Roth, M. Jin, A. E. Minovich, S. Liu, G. Li, A. V. Zayats, *Nano Lett.* **2020**, *20*, 4481; b) R. J. Ng, X. M. Goh, J. K. Yang, *Opt. Express* **2015**, *23*, 32597.
- [10] M. Song, D. Wang, S. Peana, S. Choudhury, P. Nyga, Z. A. Kudyshev, H. Yu, A. Boltasseva, V. M. Shalaev, A. V. Kildishev, *Appl. Phys. Rev.* **2019**, *6*, 041308.
- [11] A. E. Minovich, M. Peter, F. Bleckmann, M. Becker, S. Linden, A. V. Zayats, *Nano Lett.* **2017**, *17*, 4189.
- [12] A. E. Minovich, A. V. Zayats, *ACS Photonics* **2018**, *5*, 1755.
- [13] a) P. Liu, L. Bai, J. Yang, H. Gu, Q. Zhong, Z. Xie, Z. Gu, *Nanoscale Adv.* **2019**, *1*, 1672; b) J. W. Stewart, G. M. Akselrod, D. R. Smith, M. H. Mikkelsen, *Adv. Mater.* **2017**, *29*, 1602971; c) D. Franklin, Z. He, P. Mastranzo Ortega, A. Safaei, P. Cencillo-Abad, S. T. Wu, D. Chanda, *Proc. Natl. Acad. Sci. USA* **2020**, *117*, 13350.
- [14] L. Wang, R. J. H. Ng, S. Safari Dinachali, M. Jalali, Y. Yu, J. K. W. Yang, *ACS Photonics* **2016**, *3*, 627.
- [15] a) A. Murphy, Y. Sonnefraud, A. V. Krasavin, P. Ginzburg, F. Morgan, J. McPhillips, G. Wurtz, S. A. Maier, A. V. Zayats, R. Pollard, *Appl. Phys. Lett.* **2013**, *102*, 103103; b) J. McPhillips, A. Murphy, M. P. Jonsson, W. R. Hendren, R. Atkinson, F. Höök, A. V. Zayats, R. J. Pollard, *ACS Nano* **2010**, *4*, 2210.
- [16] H. Ni, M. Wang, T. Shen, J. Zhou, *ACS Nano* **2015**, *9*, 1913.
- [17] S. Wu, Y. Ye, Y. Gu, L. Chen, *Opt. Express* **2019**, *27*, 9570.
- [18] M. A. van de Haar, R. Maas, B. Brenny, A. Polman, *New J. Phys.* **2016**, *18*, 043016.
- [19] M. W. Knight, N. S. King, L. Liu, H. O. Everitt, P. Nordlander, N. J. Halas, *ACS Nano* **2014**, *8*, 834.
- [20] a) G. V. Odintsova, E. A. Vlasova, Y. M. Andreeva, M. K. Moskin, A. S. Krivososov, E. V. Gorbunova, D. V. Pankin, O. S. Medvedev, M. M. Sergeev, N. N. Shchedrina, D. S. Lutoshina, V. P. Veiko, *Opt. Express* **2019**, *27*, 3672; b) H. Liu, H. Yang, Y. Li, B. Song, Y. Wang, Z. Liu, L. Peng, H. Lim, J. Yoon, W. Wu, *Adv. Opt. Mater.* **2019**, *7*, 1801639.
- [21] M. Abdolahi, H. Jiang, B. Kaminska, *Nanotechnology* **2019**, *30*, 405301.
- [22] a) S. D. Rezaei, J. Ho, A. Naderi, M. T. Yaraki, T. Wang, Z. Dong, S. Ramakrishna, J. K. W. Yang, *Adv. Opt. Mater.* **2019**, *7*, 1900735; b) D. Chen, T. Wang, G. Song, Y. Du, J. Lv, X. Zhang, Y. Li, L. Zhang, J. Hu, Y. Fu, R. Jordan, *ACS Appl. Mater. Interfaces* **2019**, *11*, 41668.
- [23] H. Jiang, B. Kaminska, H. Porras, M. Raymond, T. Kapus, *Adv. Opt. Mater.* **2019**, *7*, 1900237.
- [24] a) C. Williams, G. S. D. Gordon, T. D. Wilkinson, S. E. Bohndiek, *ACS Photonics* **2019**, *6*, 3132; b) J. U. Salmon-Gamboa, M. Romero-Gomez, D. J. Roth, A. V. Krasavin, P. Wang, W. Dickson, A. V. Zayats, *Nanoscale Adv.* **2021**, *3*, 767.
- [25] B. Hatton, L. Mishchenko, S. Davis, K. H. Sandhage, J. Aizenberg, *Proc. Natl. Acad. Sci. USA* **2010**, *107*, 10354.